

Higher-Order Discontinuous Galerkin Method for Aeroacoustic Wave Propagation on Distorted Grids

H. Özdemir

Department of Mechanical Engineering, University of Twente
P.O. Box 217, 7500 AE, Enschede, The Netherlands
h.ozdemir@ctw.utwente.nl

H.W.M. Hoeijmakers

Department of Mechanical Engineering, University of Twente
P.O. Box 217, 7500 AE, Enschede, The Netherlands
h.w.m.hoeijmakers@ctw.utwente.nl

ABSTRACT

A high-order implementation of the Discontinuous Galerkin (DG) method is presented for solving the three-dimensional Linearized Euler Equations on an unstructured hexahedral grid. The method is based on a quadrature-free implementation and the high-order accuracy is obtained by employing higher-degree polynomials as basis functions. In the DG method the solution domain is divided into a set of non-overlapping elements and the approximate solution is expressed as a linear combination of linearly independent basis functions. The degree of the polynomials that constitute the basis functions determines the order of the accuracy of the method and, if desired, the degree can vary from element to element. The weak formulation of the problem is approximated by replacing the solution space by the space spanned by the basis functions. Hence the approximate solution, represented as an expansion in terms of basis functions, is discontinuous at the interfaces between neighboring elements. To provide the crucial coupling and to handle the discontinuity at element interfaces the boundary-normal flux is replaced by the approximate Riemann flux which is the only means by which neighboring elements communicate, regardless of the order of the method. In the present work the Riemann flux is approximated by a Lax-Friedrichs flux. For the time discretization a four-stage Runge-Kutta scheme is used which, for the present linear problem, possesses fourth-order accuracy in time. The present DG method is implemented for an unstructured hexahedral grid and is up to fourth-order accurate in space. Non-reflecting boundary conditions are implemented at the boundaries of the computational domain.

A high-order implementation of the DG method has been presented previously for solving the three-dimensional Linearized Euler Equations on an unstructured hexahedral grid with the shape of the elements restricted to parallelepipeds, for the sake of retaining a linear transformation from physical to computational coordinates. The effect of non-parallelepiped elements, i.e. of grid distortion is investigated considering two cases: a skewed and a randomly distorted mesh. The numerical dispersion due to a slope discontinuity in the initial solution is also investigated in this study.

1.0 INTRODUCTION

Compared to computational fluid dynamics the accuracy of numerical methods for aeroacoustics require more attention in the sense that numerical dispersion and dissipation errors are much more critical. Although finite-difference methods could be used to achieve higher-order accuracy, they need special treatment at the boundaries and usually require smooth, structured meshes. Especially when the problem of interest involves complex geometries this requirement cannot be met. The Discontinuous Galerkin (DG) method^{1,2} has some remarkable advantages with respect to flexibility in discretization of domains with complex geometries. The DG method is a highly compact finite-element projection method which provides a practical framework for the development

Özdemir, H.; Hoeijmakers, H.W.M. (2007) Higher-Order Discontinuous Galerkin Method for Aeroacoustic Wave Propagation on Distorted Grids. In *Computational Uncertainty in Military Vehicle Design* (pp. 40-1 – 40-18). Meeting Proceedings RTO-MP-AVT-147, Paper 40. Neuilly-sur-Seine, France: RTO. Available from: <http://www.rto.nato.int>.

Higher-Order Discontinuous Galerkin Method for Aeroacoustic Wave Propagation on Distorted Grids

of a higher-order method desired for computational aeroacoustics on non-smooth unstructured grids.³⁻¹¹ In recent studies it has been shown that the accuracy is of order larger than $p + 1/2$, while the spatial dispersion error is of order $2p + 3$ and the spatial dissipation error is of order $2p + 2$.^{12,13} The treatment of the boundary conditions is relatively simple (no special treatment required), and obtaining uniform high-order accuracy at the boundaries involving complex geometries is feasible. In the present paper a high-order implementation of the DG method is presented for solving the three-dimensional Linearized Euler Equations on an unstructured hexahedral grid. The method is based on a quadrature-free implementation and the high-order accuracy is obtained by employing higher-degree polynomials as basis functions.

2.0 QUADRATURE FREE DISCONTINUOUS GALERKIN METHOD

We consider the following three-dimensional Linearized Euler Equations (LEE):

$$L(\mathbf{u}) = \frac{\partial \mathbf{u}}{\partial t} + \frac{\partial \mathbf{f}_i(\mathbf{u})}{\partial x_i} = \mathbf{s}, \quad \mathbf{x} \in \Omega, \quad t \in I_t, \quad (1)$$

with initial and boundary conditions and,

$$\mathbf{f}_i(\mathbf{u}) = A_i(\mathbf{u}_0)\mathbf{u}, \quad A_i \in \mathbb{R}^5 \times \mathbb{R}^5, \quad A_i(\mathbf{u}_0) = \begin{bmatrix} u_{0i} & \delta_{i1}\rho_0 & \delta_{i2}\rho_0 & \delta_{i3}\rho_0 & 0 \\ 0 & u_{0i} & 0 & 0 & \delta_{1i}/\rho_0 \\ 0 & 0 & u_{0i} & 0 & \delta_{2i}/\rho_0 \\ 0 & 0 & 0 & u_{0i} & \delta_{3i}/\rho_0 \\ 0 & \delta_{i1}\gamma p_0 & \delta_{i2}\gamma p_0 & \delta_{i3}\gamma p_0 & u_{0i} \end{bmatrix}, \quad i = 1, 2, 3, \quad (2)$$

where \mathbf{u}_0 is the reference state vector, $\mathbf{s} \in \mathbb{R}^5$ is the source term, $\Omega \in \mathbb{R}^3$ is an open domain with boundary $\partial\Omega$ and $t \in I_t$ denotes time, where $I_t \in \mathbb{R}^+ \setminus \{0\}$. Furthermore, the matrices A_i , $i = 1, 2, 3$, are real and have real eigenvalues, i.e., the system is hyperbolic. At $t = 0$ initial conditions are applied. The solution vector $\mathbf{u} : \Omega \times I_t \mapsto \mathbb{R}^5$ is given by $\mathbf{u} = (\rho', u'_1, u'_2, u'_3, p')^T$, where the components of the vector denote the dimensionless perturbations of the primitive variables: density, three components of velocity and pressure, respectively. Note that the formulation presented above is not restricted to isentropic flow and entropy waves are allowed.

We discretize the Linearized Euler equations (LEE) (Eq. 1) in space, employing the Discontinuous Galerkin (DG) method in a region Ω . We consider a solution $\mathbf{u}(\cdot, t)$ such that for each time $t \in I_t$, $\mathbf{u}(\cdot, t)$ belongs to the function space U of the form $\mathbf{u}(\cdot, t) \in U^5$, $U \equiv L^2(\Omega)$, where $L^2(\Omega)$ denotes a Hilbert space of all square integrable functions on Ω with an associated inner product $\langle \cdot, \cdot \rangle$. The weak formulation of the LEE can be written as

$$\langle L(\mathbf{u}(\cdot, t)), \mathbf{v} \rangle = \langle \mathbf{s}, \mathbf{v} \rangle, \quad \forall \mathbf{v} \in U^5. \quad (3)$$

In order to discretise the LEE we divide the solution domain Ω into non-overlapping hexahedral elements Ω_j such that $\bar{\Omega} = \bigcup_{j=1}^{N_e} \bar{\Omega}_j$, where $\bar{\Omega}_j = \Omega_j \cup \partial\Omega_j$ is the closure of Ω_j and the boundary $\partial\Omega_j$ belongs to at most two elements and N_e denotes the number of elements. In the semi-discrete formulation we consider the approximation $\mathbf{u}_h(\cdot, t)$, of the solution $\mathbf{u}(\cdot, t)$ as an expansion onto the basis set $\{b_{jk}\}$

$$\mathbf{u}_h(\mathbf{x}, t) = \sum_{j=1}^{N_e} \mathbf{u}_{jk}(t) b_{jk}(\mathbf{x}), \quad (4)$$

with, $\mathbf{u}_{jk} \in L^2(I_t)$ and $b_{jk} \in L^2(\Omega)$. It is noted that we employ the Einstein summation convention, except for the index "j". The \mathbf{u}_{jk} are the solution expansion coefficients of the solution on Ω_j and functions of time only. The functions $\{b_{jk}\}$ are linearly independent basis functions defined such that

$$b_{jk} \equiv \begin{cases} \bar{b}_{jk}(\mathbf{x}), & \mathbf{x} \notin \partial\Omega_j, \\ 0, & \mathbf{x} \in \partial\Omega_j, \end{cases}, \quad \bar{b}_{jk}(\mathbf{x}) = 0, \quad \mathbf{x} \notin \bar{\Omega}_j, \quad (5)$$

The functions \bar{b}_{jk} and b_{jk} differ only in that $b_{jk} = 0$ on the boundary $\partial\Omega_j$ while in general $\bar{b}_{jk} \neq 0$ on the boundary $\partial\Omega_j$. The basis functions are continuous in Ω_j and $k = 0, 1, \dots, M$ is the index of the polynomials where the upper limit is defined as;

$$M(p, d) = \frac{1}{d!} \prod_{l=1}^d (p + l), \quad (6)$$

with d the number of space dimensions and p the highest degree of the polynomials used. We approximate the weak formulation (Eq. (3)) by:

$$\langle L(\mathbf{u}_h(\cdot, t)), b_{jm} \rangle = \langle \mathbf{s}, b_{jm} \rangle, \quad \forall j \in (1, 2, \dots, N_e), \quad \forall m \in (0, 1, \dots, M). \quad (7)$$

Using Eqs.(1), upon partial integration and applying Gauss' theorem we evaluate Eq.(7) for every basis function b_{jm} ,

$$\int_{\Omega_j} \frac{\partial \mathbf{u}_{jk}}{\partial t} b_{jk} b_{jm} d\Omega - \int_{\Omega_j} \mathbf{f}_{ji} \frac{\partial b_{jm}}{\partial x_i} d\Omega + \int_{\partial\Omega_j} b_{jm} \mathbf{f}_{ji} n_{ji} dS = \int_{\Omega_j} \mathbf{s} b_{jm} d\Omega. \quad (8)$$

where $\mathbf{f}_{ji} \equiv A_i \mathbf{u}_{jk} b_{jk}$. At any interface between two elements, since the solution is allowed to be discontinuous, there is a left state and a right state, leading to a Riemann problem. Solving the Riemann problem will handle the discontinuity at element interfaces and provide the coupling at the element interfaces. Various kinds of flux formulas have been proposed and used in the literature to approximate the Riemann problem. In this study we employ the *Lax-Friedrich* flux formula of the form

$$\mathbf{h}(\mathbf{u}^L, \mathbf{u}^R, \mathbf{n}) = \frac{1}{2} \{ \mathbf{f}(\mathbf{u}^L) + \mathbf{f}(\mathbf{u}^R) - \theta |a|_{max} (\mathbf{u}^R - \mathbf{u}^L) \}, \quad \theta \geq 0, \quad (9)$$

where, $|a|_{max}$ is the maximum (absolute value) of the eigenvalues of the (5×5) matrix \mathbf{A}_i , \mathbf{u}^L and \mathbf{u}^R are the values of the \mathbf{u}_{jk} at the interface calculated using expansion coefficients of the elements at the left and right of that interface.

The basis functions are defined on the "master" or "reference" element $\hat{\Omega}$, in the computational space. The local coordinates in the master element are given by $\boldsymbol{\xi} = (\xi, \eta, \zeta)^T$ and the coordinate system has its origin at the centroid of the hexahedron $\hat{\Omega} \equiv (-1, 1)^3$. The physical coordinates in element Ω_j are related to the computational coordinates in $\hat{\Omega}$ by a map $\mathbf{x}^j(\boldsymbol{\xi})$ and an inverse map $\boldsymbol{\xi}^j(\mathbf{x})$. Assuming that the physical elements are restricted to parallelepiped, both maps are linear, but for a constant. On $\hat{\Omega}$ we define a set of linearly independent polynomials $\{b_k(\xi, \eta, \zeta)\}$ of degree $\leq p$:

$$\{b_k\} = \{ \xi^{k_1} \eta^{k_2} \zeta^{k_3} \mid 0 \leq k_1 + k_2 + k_3 \leq p, \quad k_i \geq 0 \}. \quad (10)$$

The compactness of the method results in an easy implementation of the boundary conditions. The boundary conditions can be implemented by prescribing the exact external solution (\mathbf{u}_R) or by reformulating the Lax-Friedrichs flux in terms of the interior solution (\mathbf{u}_L) and the physical boundary conditions. For the current implementation characteristics-based non-reflecting and symmetry-plane boundary conditions are used as described by Atkins.³

The time integration is performed by a four-step, low storage Runge-Kutta algorithm¹⁴ which is known to be fourth-order accurate for linear problems. LeSaint and Raviart¹⁵ made the first analysis of the Discontinuous Galerkin method and proved a rate of convergence of at least h^p for general triangulations and of h^{p+1} for Cartesian grids employing basis polynomials up to order p , where h is a length scale that represents the size of elements. Later, Johnson and Pitkäranta¹ proved a rate of convergence of at least $h^{p+\frac{1}{2}}$ for general triangulations and Peterson¹⁶ numerically confirmed that this rate of convergence cannot be improved within the class of quasi-uniform meshes. Richter¹⁷ obtained the optimal rate of convergence of h^{p+1} for a semi-uniform triangulation. Hence, when the method is applied to a hexahedral mesh, the analysis of LeSaint and Raviart

Higher-Order Discontinuous Galerkin Method for Aeroacoustic Wave Propagation on Distorted Grids

indicates that the method is $(p + 1)^{th}$ -order accurate.

3.0 GRID DISTORTION

3.1 Acoustic Radiation from a Vibrating Wall Segment

Consider an infinite rectangular duct of height $h = 1$ and width b , see figure (1). In the middle of the duct a finite part of the duct bottom wall, of length $2l$, is allowed to vibrate. The origin of the Cartesian coordinate system is in the mid-section of the duct at one of the lower corners. In the origin we define the orthogonal unit coordinate vectors \mathbf{e}_x , \mathbf{e}_y and \mathbf{e}_z . In the present paper we consider the sound field generated by this vibrating wall segment inside the infinite duct. It is assumed that the problem can be described by the (non-dimensionalized) linearized Euler equations.

The wall can be described by the position vector \mathbf{x}_s (for $t > 0$) on the moving surface ($S = 2l \times b$):

$$\mathbf{x}_s(x, y, t) = x\mathbf{e}_x + y\mathbf{e}_y + z_s(x, y, t)\mathbf{e}_z, \quad x \in [-l, l], \quad y \in [0, b]. \quad (11)$$

The velocity vector \mathbf{U} is given by:

$$\mathbf{U}(x, y, z, t) = (M + u')\mathbf{e}_x + v'\mathbf{e}_y + w'\mathbf{e}_z, \quad x \in [-\infty, \infty], \quad y \in [0, b], \quad (12)$$

where M is the Mach number. Since the surface is assumed to be impenetrable, flow may not pass through the wall. This can be imposed by means of the kinematic condition $\frac{dF}{dt} = 0$, where $F(x, y, z, t) \equiv z_s(x, y, t) - z$ is the definition of the moving surface:

$$\begin{aligned} \left(\frac{dF}{dt}\right)_s = 0 &\Rightarrow \left[\frac{\partial F}{\partial t} + \frac{d\mathbf{x}_s}{dt} \cdot \nabla F\right]_s = 0, \\ &\Rightarrow \left[\frac{\partial F}{\partial t} + \mathbf{U} \cdot \nabla F\right]_s = 0. \end{aligned} \quad (13)$$

With

$$\frac{\partial F}{\partial t} = \frac{\partial z_s}{\partial t}, \quad \nabla F = \frac{\partial z_s}{\partial x}\mathbf{e}_x + \frac{\partial z_s}{\partial y}\mathbf{e}_y - \mathbf{e}_z, \quad (14)$$

we obtain:

$$\left[\frac{\partial z_s}{\partial t} + (M + u')\frac{\partial z_s}{\partial x} + v'\frac{\partial z_s}{\partial y} - w'\right]_s = 0, \quad x \in [-l, l], \quad y \in [0, b], \quad z = z_s(x, y, t) \quad (15)$$

We assume that the amplitude of the surface displacement is small ($\mathcal{O}(\epsilon)$) compared to the acoustic wave length and the surface dimensions, $2l \times b$. Based on these assumptions it is consistent to linearize Eq.(15) with respect to the stationary reference surface $z = 0$ (Pierce¹⁸). This leads to:

$$w'(x, y, 0, t) = \frac{\partial z'_s}{\partial t} + M\frac{\partial z'_s}{\partial x} + \mathcal{O}(\epsilon^2). \quad (16)$$

The perturbation velocity induced by the wall motion is scaled, i.e. $w = w'/\epsilon$. In addition also the small surface displacement will be rescaled $z_s = z'_s/\epsilon$. The displacement of the surface results in a normal velocity boundary condition for the linearized Euler equations for part of the bottom surface $z = 0$, which can be expressed as:

$$u_n(x, y, t) = \psi(x, y, t)H(l - |x|), \quad x \in (-\infty, \infty), \quad y \in [0, b], \quad (17)$$

where

$$\psi(x, y, t) \equiv w'(x, y, 0, t) = \left(\frac{\partial z_s}{\partial t} + M\frac{\partial z_s}{\partial x}\right), \quad (18)$$

and where H is the Heaviside function and l is dimensionless and finite.

The non-dimensionalized convected wave equation can be derived for the pressure as follows:

$$\frac{D^2 p}{Dt^2} - \nabla^2 p = 0, \quad \frac{D}{Dt} = \frac{\partial}{\partial t} + M \frac{\partial}{\partial x}, \quad \nabla^2 = \frac{\partial^2}{\partial x^2} + \frac{\partial^2}{\partial y^2} + \frac{\partial^2}{\partial z^2}. \quad (19)$$

Taking the inner product of the momentum equation with the unit normal $\mathbf{n}_0 = -\mathbf{e}_z$, results in the following linearized boundary condition for the pressure at $z = 0$:

$$\frac{\partial p}{\partial z} \Big|_{z=0} = - \left(\frac{\partial u_n}{\partial t} + M \frac{\partial u_n}{\partial x} \right). \quad (20)$$

On the other walls, which are rigid and impenetrable, we apply the hard-wall conditions:

$$\frac{\partial p}{\partial z} \Big|_{z=1} = 0, \quad \frac{\partial p}{\partial y} \Big|_{y=0} = 0, \quad \frac{\partial p}{\partial y} \Big|_{y=b} = 0. \quad (21)$$

In the following sections we will solve Eq.(19) with the boundary conditions given by Eq.(20) and Eq.(21).

Let us assume that the displacement of the vibrating wall segment is represented by the following function (see Eq. (17)):

$$\psi(t) = \sin(\omega_0 t) e^{-at} H(t), \quad (22)$$

where H is the Heaviside function. In this case the whole vibrating plate ($-l \leq x \leq l$), ($0 \leq y \leq b$) moves up and down as a rigid body in a damped sinusoidal motion (see figure (1)). The simulations have been performed for $\omega_0 = \frac{4}{3}$, $l = 2.5$ and $a = 0.05$.

In previous studies^{9,11} regular (undistorted) hexahedral elements were used in the numerical algorithm, with the shape of the elements restricted to parallelepipeds, for the sake of retaining a linear transformation from physical to the computational coordinates. It is clear that for solution domains with complex geometries we have to resort to more general hexahedral elements and the approach of a linear(ized) transformation will be inadequate, or rather constitutes an approximation. In this study the effect of non-parallelepiped elements, i.e. of grid distortion is investigated considering two cases. In the first case the grid is skewed at a certain angle while keeping the shape of the elements as parallelepiped and in the second case the grid is randomly distorted, violating the restriction to parallelepiped elements. In the skewed mesh case both the *inflow* and the *outflow* boundaries of the domain are also skewed while in the randomly distorted mesh the domain boundaries are retained as (y,z)-planes. In all cases we take $\omega_0 = \frac{4}{3}$, $l = 2.5$ and $a = 0.05$. In the following sections the effect of grid distortion is analyzed for the two types of grid distortion considered and the numerical results are discussed.

3.2 Skewed Mesh

The faces of the solution domain that coincide with $y = \text{constant}$ plane are skewed at a certain angle " α " and then partitioned into equally sized cells with opposite faces that are parallel. The mesh is shown in figure (1). In total three skew angles have been considered namely $\alpha = 2.5$, $\alpha = 5$ and $\alpha = 10$ deg.

The simulations have been performed for a quiescent background ($M = 0$). For the skewed mesh case the problem cannot be assumed geometrically symmetrical with respect to the $x = 0$ plane, thus the whole domain is considered. The parallelepiped domain is given by $x \in [-10 + z \tan \alpha, 10 + z \tan \alpha]$, $y \in [0, \Delta y]$ and $z \in [0, 1]$, where all lengths are non-dimensional and Δy is the size of the element in y -direction. At the end planes of the duct, the characteristics non-reflecting boundary conditions are applied, while solid-wall boundary conditions are applied at the other walls except the vibrating wall segment. The location of $x_{max}(= \pm 10)$ is chosen such that the waves originating from the vibrating wall segment do not reach the boundary in the time considered in the simulation. The hexahedral mesh is obtained as explained above. The problem is two-dimensional but the method for three-dimensional wave-propagation problems is applied to obtain the numerical results.

Higher-Order Discontinuous Galerkin Method for Aeroacoustic Wave Propagation on Distorted Grids

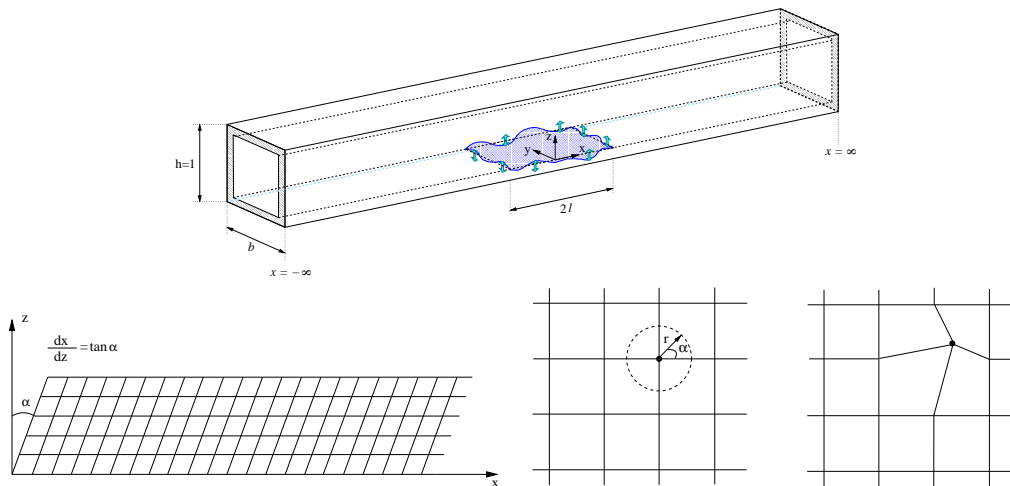


Figure 1. Sketch of a problem (top) and distorted grids (bottom) left: skewed mesh, right: randomly distorted mesh, $b = \Delta y$, $l = 2.5$ and the channel length is 20.0

During the computations the solution is obtained at the cell centers and subsequently as a post-processing the values at all element corner points are evaluated using the basis functions. This implies that at a given node point we have up to 8 values, one time each element that has that specific node point at one of its corner points. The node values are then obtained by averaging over all these values. Additionally a time history of the perturbation variables is recorded at certain locations (not necessarily a node point or a centroid) throughout the rectangular duct. These locations are called *microphone* locations. The solution at the microphone location is obtained directly from the solution using the basis functions.

In figure (2) the time histories of the pressure perturbation is plotted showing a comparison between the results for various values of the grid distortion angle for the finest mesh considered at $(x = 3.0125, y = \Delta y/2, z = 0.0125)$ and $(x = 9.0125, y = \Delta y/2, z = 0.0125)$. These microphone positions are chosen such that they are at the centroid of an element of the finest mesh and away from the edges of the elements of the coarser meshes. If the solution for $\alpha = 0$ (undistorted case) is taken as a reference then it can be concluded that when increasing the grid distortion angle the deviation from the pressure history for the undistorted case increases gradually. These time histories of the pressure perturbations at a location close to the vibrating segment, i.e. left-hand side of figure (2), clearly show the wave originating from the oscillatory segment and the wave reflected from the top wall. At the location further away from the vibrating segment the wave is almost one-dimensional.

In the left hand side of figure (3) contour plots for the pressure perturbation in the plane $y = \Delta y/2$ for $t = 0.8$ to 7.2 are shown while in the right hand side the pressure perturbations along the (horizontal) line $y = \Delta y/2, z = 0.25$ as well as along the (vertical) line $x = 0, y = \Delta y/2$ are plotted. This data is for the mesh with $800 \times 1 \times 40$ elements in x -, y - and z -directions, respectively. Above, as well as close to the vibrating wall segment, a relatively complex pattern develops, while away from this segment plane waves evolve.

3. 2. 1 Accuracy

In the preceding section the effect of the skewness angle α is shown in terms of details of the perturbation pressure field. The following analysis is conducted to assess the effect of the grid distortion parameter in terms of L_2 -norms of differences between the time histories at two microphone locations. For each angle $\alpha_0 (= 0)$, α_1 , α_2 and α_3 and for each mesh size h_1 , h_2 and h_3 , with h_1 the coarsest and h_3 the finest mesh, we have signal $p'(t; h_i, \alpha_j)$, i.e. there are 12 signals in total for each microphone position considered. Taking the result of the simulation for $h_3, \alpha = 0$ as a reference solution the L_2 -norm of the difference ("error") with respect to this solution can be calculated for each angle and mesh size considered, as follows:

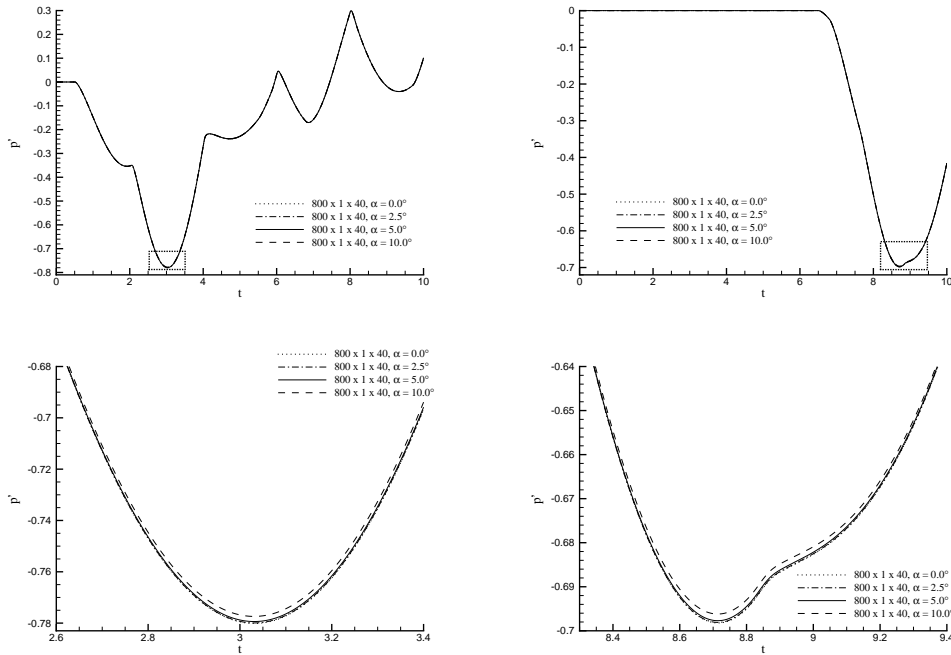


Figure 2. Vibrating wall segment $x \in [-2.5, 2.5]$, $y \in [0, b]$, $z = 0$, $\omega_0 = \frac{4}{3}$, $l = 2.5$, $a = 0.05$. Comparison of the time histories of p' at $(x = 3.0125, y = \Delta y/2, z = 0.0125)$ (top left) and p' at $(x = 9.0125, y = \Delta y/2, z = 0.0125)$ (top right) for $800 \times 1 \times 40$ mesh for various values of grid skewness angle α . Detailed views (bottom left and bottom right). The order of approximation is $p = 3$.

$$\|\varepsilon\|_{ij} = \sqrt{\frac{1}{T} \int_0^T \{p'(t; h_i, \alpha_j) - p'(t; h = h_3, \alpha_0 = 0)\}^2 dt} \quad (23)$$

The integral in Eq. (23) is approximated by Gaussian quadrature for $0 \leq t \leq T = 10$ using a fixed Δt of 1.0×10^{-3} .

The left hand side of figure (4) shows the error as function of the angle α for the mesh sizes considered for the order of accuracy $p = 1$ and the right hand side for the order of accuracy $p = 3$. It is clear from these figures that the "error" decreases with increasing order of accuracy as expected. It can be concluded that for each order, for each mesh considered, the difference increases with increasing grid distortion. The order of magnitude of the effect of grid distortion, for small grid distortions, is of the same order of magnitude as the difference between solutions for different mesh sizes.

3.3 Randomly Distorted Mesh

In the randomly distorted grid case the elements are not restricted to parallelepipeds, which differs from the case considered in the preceding section. The hexahedral base mesh is obtained by partitioning the physical domain into equally sized cubes.

For each grid point that does not coincide with the boundary an angle " θ " and a radius " r " are chosen randomly and the new coordinate of the grid point is calculated with the distortion $(\Delta x, \Delta y)^T = r(\cos\theta, \sin\theta)^T$. The values of r are limited to 2.5, 5 and 10% of the length of the cell edge, here referred to as the distortion parameter " d ". The right hand side of figure (1) shows the distorted grid after one grid point has been processed.

As can be seen from the figures the grid generated in this way is 2D. Recall that the numerical algorithm used to solve the linearized Euler equations solves the problem in 3D. To keep the 2D nature of the problem the grid

Higher-Order Discontinuous Galerkin Method for Aeroacoustic Wave Propagation on Distorted Grids

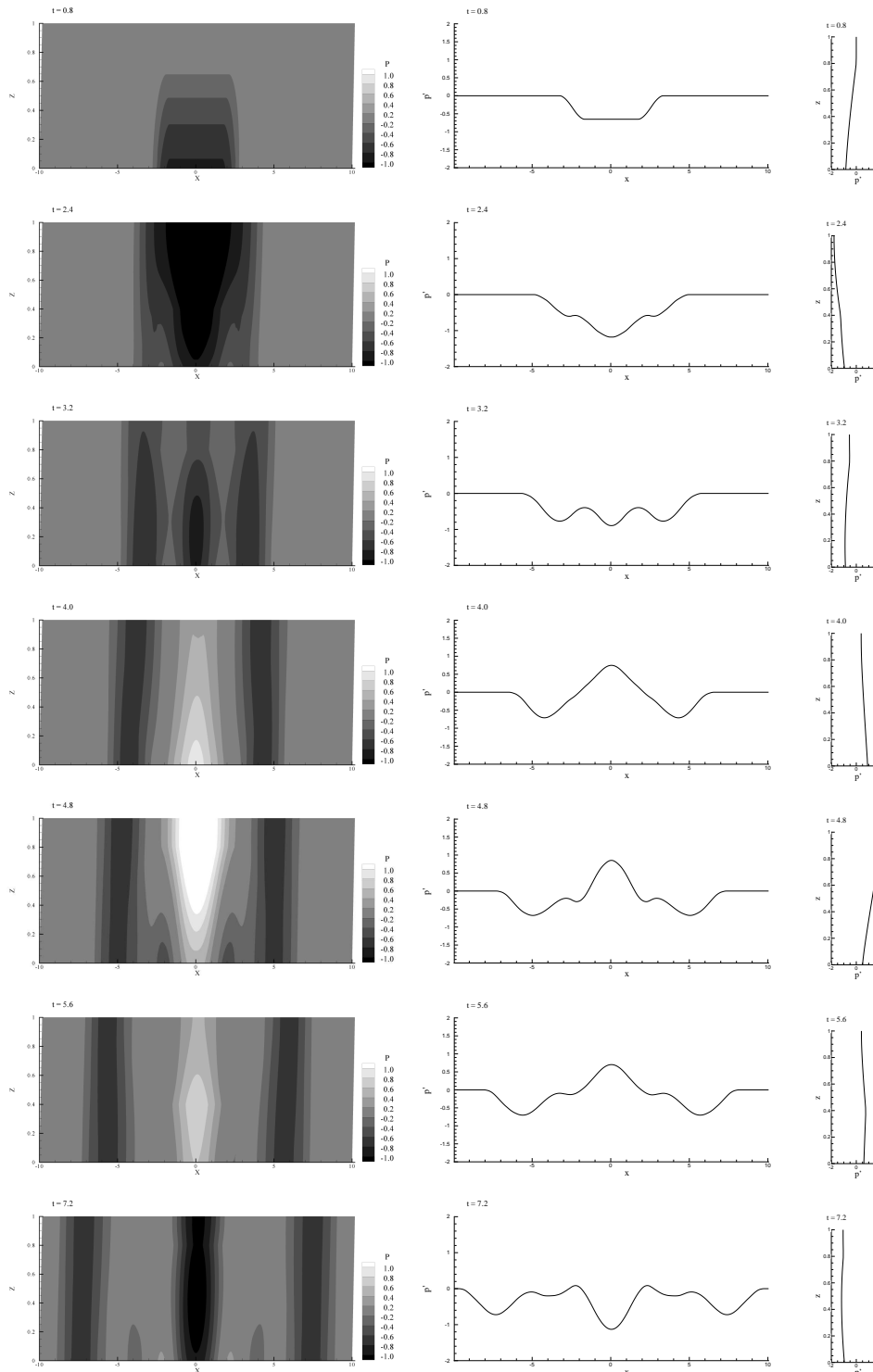


Figure 3. Vibrating wall segment $x \in [-2.5, 2.5]$, $y \in [0, b]$, $z = 0$, $\omega_0 = \frac{4}{3}$, $l = 2.5$, $a = 0.05$, $\alpha = 10$ deg. Left: Contour plots for the pressure perturbation in the plane $y = \Delta y/2$ for $t = 0.8$ to 7.2 . Middle: Pressure perturbation along line ($y = \Delta y/2$, $z = 0.25$). Right: Pressure perturbation along line ($x = 0$, $y = \Delta y/2$). $\Delta x = \Delta y = \Delta z = 0.025$, $\Delta t = 1.0 \cdot 10^{-3}$.

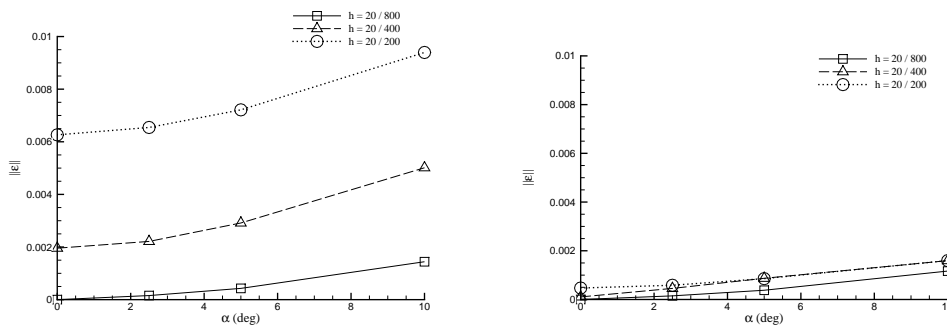


Figure 4. Results for vibrating wall segment $x \in [-2.5, 2.5]$, $y \in [0, b]$, $z = 0$, $\omega_0 = \frac{4}{3}$, $l = 2.5$, $a = 0.05$. L_2 -norm of difference of time history of pressure perturbation with that of reference solution as function of grid distortion angles for various grid sizes at location ($x = 3.0125$, $y = \Delta y/2$, $z = 0.0125$). Order of approximation is $p = 1$ (left), $p = 3$ (right).

generated in 2D is copied in the third direction while, one cell used in that direction.

The simulations are performed for a quiescent background ($M = 0$). For the randomly distorted mesh case the mesh is assumed to be symmetrical with respect to the plane $x = 0$. The rectangular domain is given by $x \in [0, 10]$, $y \in [0, \Delta y]$ and $z \in [0, 1]$, where all lengths are non-dimensional and Δy is the size of the element in y -direction. At the end planes of the duct, the characteristics non-reflecting boundary conditions are applied, while solid-wall boundary conditions are applied at the other walls except at the vibrating wall segment. The location of $x_{max}(= 10)$ is chosen such that the plane wave does not reach the boundary in the time considered in the simulation.

In figure (5), the time histories of the pressure perturbation is plotted showing a comparison between the results for various values of the distortion parameter for the finest mesh at ($x = 3.0125$, $y = \frac{1}{2}\Delta y$, $z = 0.5125$) and ($x = 9.0125$, $y = \frac{1}{2}\Delta y$, $z = 0.5125$), respectively. If the solution for the distortion parameter $d = 0$ (undistorted grid) is taken as a reference then it can be concluded that increasing the distortion parameter d , the deviation from the undistorted case increases.

In the left hand side of figure (6) contour plots for the pressure perturbation in the plane $y = \Delta y/2$ for $t = 0.8$ to 7.2 are shown, while in the right hand side the pressure perturbation along the line ($y = \Delta y/2$, $z = 0.25$), and the line ($x = 0$, $y = \Delta y/2$) are plotted. This data is for the mesh with $400 \times 1 \times 40$ elements in x -, y - and z -directions, respectively. Comparison of these results with the corresponding results for the skewed mesh show that, judging from these plots, the differences are small.

However, in the results for the randomly distorted mesh small-amplitude wiggles are present in the time-history of the pressure perturbation, figure (5), as well as in the snapshots of the pressure perturbation, figure (6). Figure (5) indicates that the amplitude increases with increasing value of the distortion parameter d . The snapshots in figure (6) are for the largest value of d considered, i.e. $d = 10$. The wavelength of the wiggles appears to correspond with the element size $\Delta x(= \Delta y = \Delta z)$. For example in the bottom figure of figure (5), for $d = 10$, the element size of the finest mesh is $\Delta x = 1/40 = 0.025$, the wavelength of the small disturbance on the time history is about $T = 2c\Delta x = 0.05$. For the snapshot, e.g. figure (6), right figure, suggests a wave length of $L = 0.1$, twice the wavelength in longitudinal direction, which will be due to the boundary conditions at the duct walls.

3. 3. 1 Accuracy

As in the preceding section the effect of the distortion parameter d is considered here in terms of the L_2 -norms of the differences in the time history at a microphone position. For each value of the distortion parameter $d_0 (=0)$, d_1 , d_2 and d_3 and for each mesh size h_1 , h_2 and h_3 we have a signal as function of time, i.e. there are 12 signals in total. Taking the result of the simulation for h_3 , $d_0 = 0$ as a reference solution the dependency of the

Higher-Order Discontinuous Galerkin Method for Aeroacoustic Wave Propagation on Distorted Grids

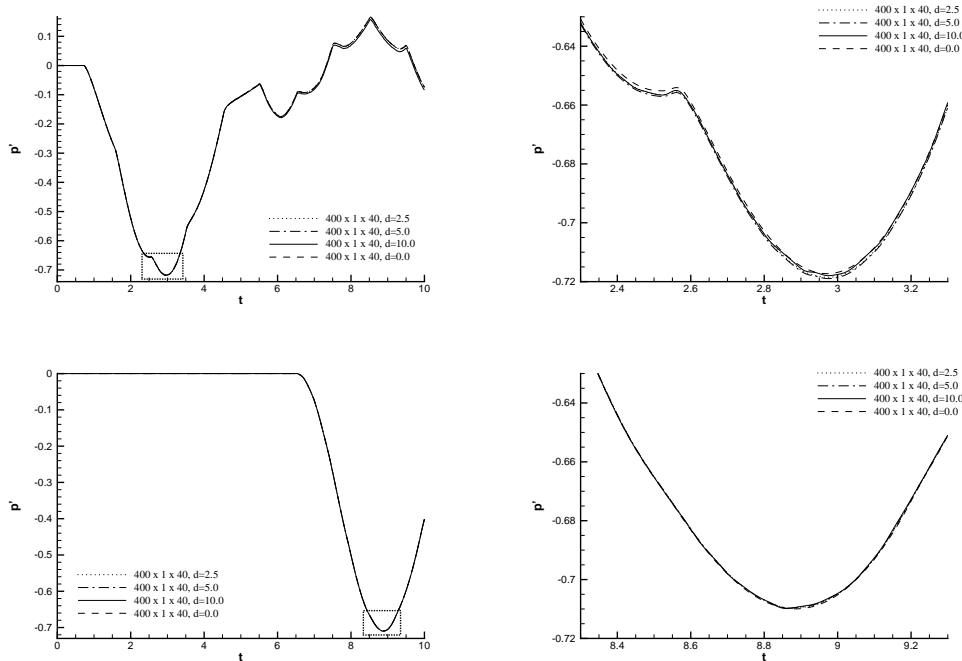


Figure 5. Vibrating wall segment $x \in [0, 2.5]$, $y \in [0, b]$, $z = 0$, $\omega_0 = \frac{4}{3}$, $l = 2.5$, $a = 0.05$. Comparison of the time histories of p' at $(x = 3.0125, y = \Delta y/2, z = 0.0125)$ (top left) and p' at $(x = 9.0125, y = \Delta y/2, z = 0.5125)$ (bottom left) for 400x1x40 mesh for various values of grid distortion parameters d (top). Detailed view (top right and bottom right). The order of approximation is $p = 3$.

difference with respect to distortion parameter can be calculated for each distortion parameter and mesh size considered, as follows:

$$\|\varepsilon\|_{ij} = \sqrt{\frac{1}{T} \int_0^T \{p'(t, h_i, d_j) - p'(t, h = h_3, d_0 = 0)\}^2 dt} \quad (24)$$

The integral is approximated using Gaussian quadrature for $0 \leq t \leq T = 10$ using a fixed Δt of 1.0×10^{-3} . The present implementation of the method is restricted to meshes with parallelepiped elements since the transformation of the elements in the physical space to the unit element in computational space is obtained by a linear approximation. This implies that the present mapping is exact for parallelepiped elements and approximate for more general elements. Using a randomly distorted mesh the restriction to parallelepiped elements is violated. In this case the linear approximation no longer holds and the truncation error due to the linear mapping can play a dominant role. The L_2 -norm of the difference for each value of the mesh size as a function of distortion parameter d for order of approximation $p = 1$ is shown in the left-hand side of figure (7) and for order of approximation $p = 3$ it is shown in the right-hand side. One may expect that with increasing order of approximation a significant decrease in the error, for a given mesh size h and distortion parameter d . From the comparison of left and right hand sides of figure (7) it is clear that for higher values of d there is no significant decrease in error with increasing order of approximation. This is because the truncation error due to the linear mapping plays a dominant role in case of meshes with non-parallelepiped elements.

4.0 Slope Discontinuity in Incoming Wave

4.1 Two Infinitely Long Alined Ducts

The present method is applied to a problem in which an infinitely long duct is split up longitudinally in two ducts by a plate. The plate has a transverse slit, referred to as an aperture here, which results in a connection

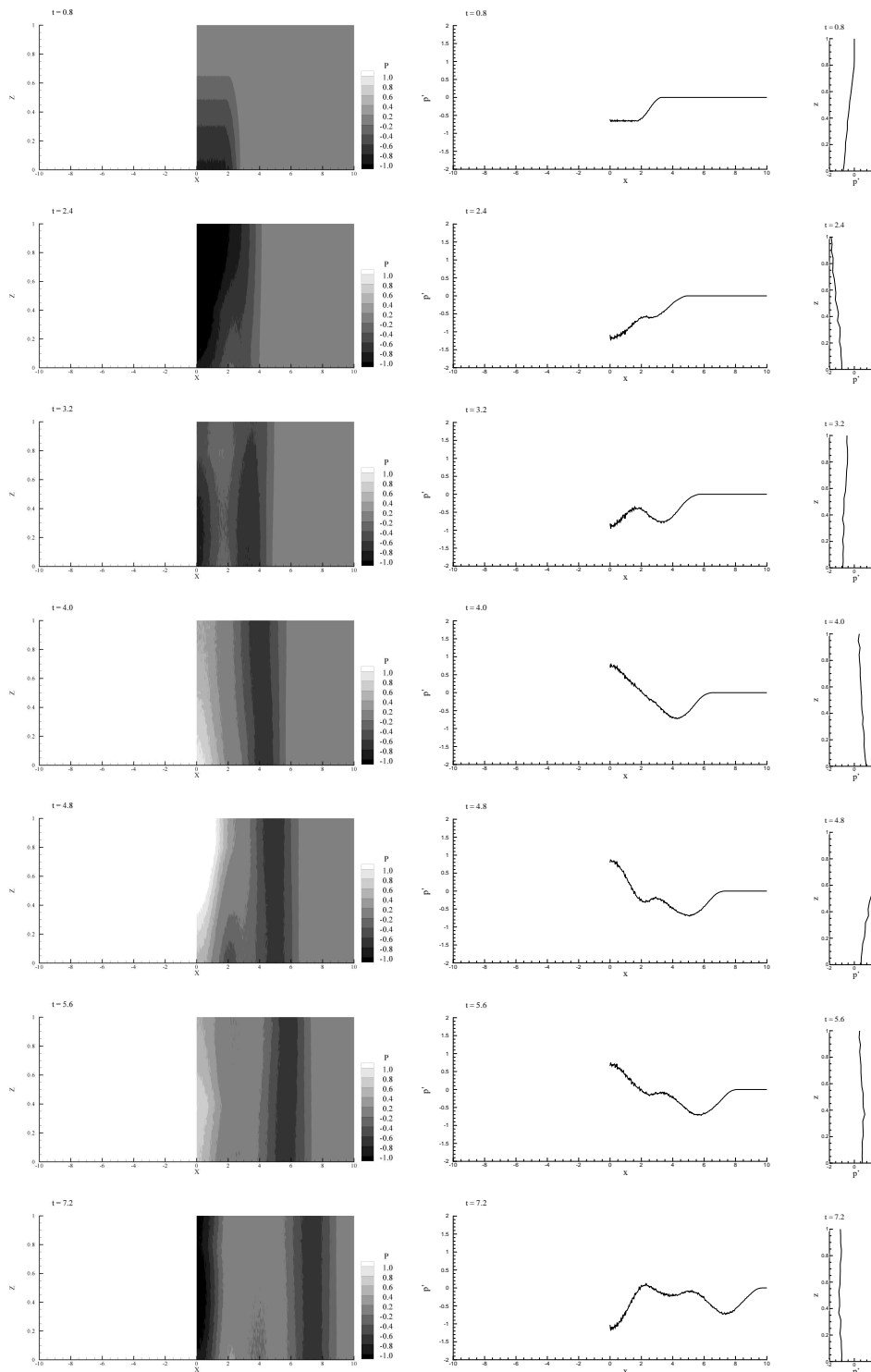


Figure 6. Vibrating wall segment $x \in [-2.5, 2.5]$, $y \in [0, b]$, $z = 0$, $\omega_0 = \frac{4}{3}$, $l = 2.5$, $a = 0.05$, $d=10$. **Left:** Contour plots for the pressure perturbation in the plane $y = \Delta y/2$ for $t = 0.8$ to 7.2 . **Middle:** Pressure perturbation along line ($y = \Delta y/2$, $z = 0.25$). **Right:** Pressure perturbation along line ($x = 0.0$, $y = \Delta y/2$). $\Delta x = \Delta y = \Delta z = 0.025$, $\Delta t = 1.0 \cdot 10^{-3}$.

Higher-Order Discontinuous Galerkin Method for Aeroacoustic Wave Propagation on Distorted Grids

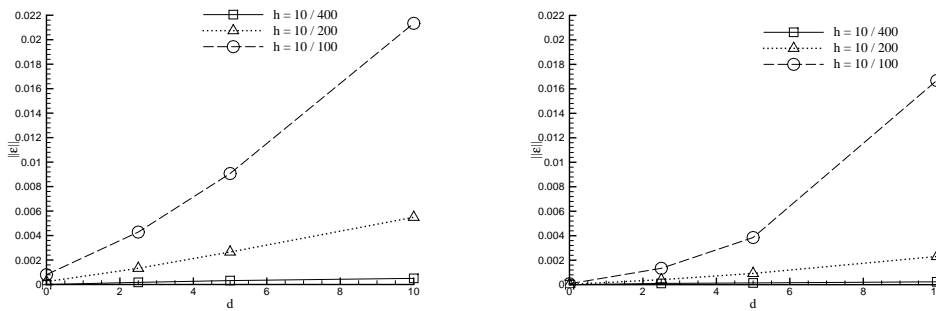


Figure 7. Results for vibrating wall segment $x \in [0, 2.5]$, $\omega_0 = \frac{4}{3}$, $l = 2.5$, $a = 0.05$. L_2 -norm of difference of pressure perturbation with reference solution as function of distortion parameters for various grid sizes at location ($x = 3.0125$, $y = \Delta y/2$, $z = 0.0125$) for order of approximations $p=1$ (left) and $p=3$ (right).

between the two parts of the duct. The configuration is depicted in figure (8). The non-dimensional height of the two parts of the duct is identical, i.e. $h/2$, where $h = (\omega/c)h'$. Here ω is the radian frequency of sound, c the speed of sound and h' a height with dimension. The non-dimensional width of the aperture is $2s = 2(\omega/c)s'$, with s' a length with a dimension. In the computation the non-dimensional length of the duct is taken to be equal to $2L = 2(\omega/c)L'$, with L' a length with dimension.

The configuration is symmetric with respect to the vertical plane $x = L$, i.e. the plane passing through the middle of the aperture. The configuration is split in 3 regions, see figure (8). Region 1 is the lower duct left and right of the aperture region. Region 2 is the upper part of the duct left and right of the aperture region. Region 3 is the aperture region, extending from the lower wall of the duct to the upper wall of the duct. An incoming wave is introduced at the open boundaries of region 2. The time histories of the perturbations on the mean flow variables are recorded at *microphones* in vertical arrays at various locations in the duct.

We choose L to be equal to $L = 3$ and h equal to $h = 2$. When the mean flow is absent ($M = 0$), the flow problem is symmetrical with respect to the plane $x = L = 3$, i.e. in that case it is sufficient to consider the left half of the configuration only. It has been verified that indeed for the no-flow case the numerical solution is symmetric with respect to the plane $x = L$ when computing the solution in the whole configuration.

In the no-flow case the rectangular domain is now given by $x \in [0, 3]$, $y \in [0, \Delta y]$ and $z \in [0, 2]$, where all lengths are non-dimensional and Δy is the size of the element in y -direction. The aperture has a half-width of $s = 0.125$. At the end planes of the duct, the characteristic non-reflecting boundary conditions are applied, while solid-wall boundary conditions are applied at the other walls.

For the present diffraction problem a sine wave is introduced as an incoming wave at the open boundary of region 2, i.e. both from the left and from the right. At the open boundary at the left the Riemann invariant corresponding to the right running characteristic, $R_1(0, y, z, t) = \rho_0 c_0 u'(0, y, z, t) + p'(0, y, z, t)$, is prescribed as $A \sin \omega t$, while the Riemann invariant corresponding to the left running characteristic, $R_2(0, y, z, t) = \rho_0 c_0 u'(0, y, z, t) - p'(0, y, z, t) = 0$. At the right open boundary we require $R_1(2L, y, z, t) = \rho_0 c_0 u'(0, y, z, t) + p'(0, y, z, t) = 0$ while $R_2(2L, y, z, t) = \rho_0 c_0 u'(0, y, z, t) - p'(0, y, z, t)$ is prescribed as $A \sin \omega t$. Various frequencies are chosen, above as well as below the cut-off frequency of the duct which is $\omega_c = \pi$. Microphones are located in four vertical arrays close to the left end of the duct, i.e. the left side of the left part of region 1 and region 2 ($x = 0.5$, $y = \Delta y/2$, $z \in [0, 1]$ and $z \in [1, 2]$, respectively) and close to the aperture ($x = 2.5$, $y = \Delta y/2$, $z \in [0, 1]$ and $z \in [1, 2]$, respectively). Each array of microphones consists of 40 microphones (a total of 160 microphones).

The analytical solution has been given by Kooijman et al.^{19,20} using a modal expansion of the pressure field in the three regions 1, 2 and 3 (see figure (8)). By matching the pressure and velocity at the interfaces between regions 1 and 3, and between regions 2 and 3, a scattering matrix for the left boundary of region 3 is obtained. This matrix relates the amplitudes of the outgoing modes p_1^-, p_2^-, p_3^+ to the amplitudes of the incoming modes p_1^+, p_2^+, p_3^- . By using these amplitudes reflection and transmission coefficients of the plane waves are calculated.

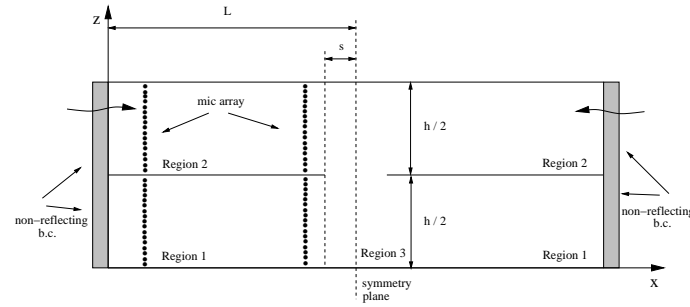


Figure 8. Infinite plate with slit inside duct.

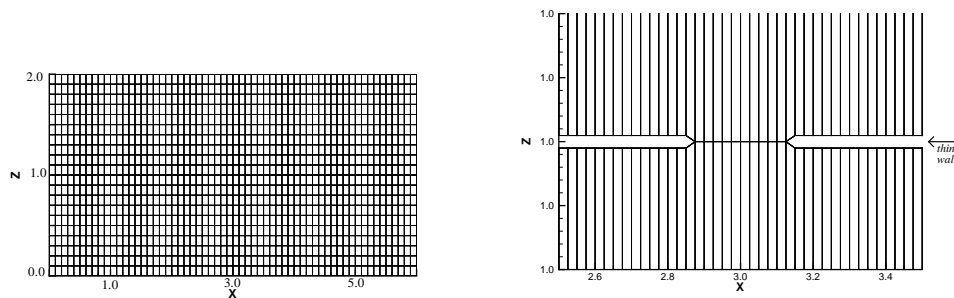


Figure 9. Complete (coarsest) mesh $\Delta x = \Delta y = \Delta z = 0.1$ (left). A close up of the (finest) mesh $\Delta x = \Delta y = \Delta z = 0.025$ around the aperture (right).

For the verification of the computational method the numerical results are compared with the analytical solution. The hexahedral mesh is obtained by partitioning the physical domain in equally sized cubes. The problem is two-dimensional but the method for three-dimensional wave-propagation problems is applied to obtain the numerical results. In order to reduce the computation time, after verifying that there is no effect of the third-direction in the numerical solution, only one cell is used in the y -direction. A detailed (not-equally scaled in x and z -directions) view of the hexahedral mesh around the aperture is included in figure (9).

Signals are array-averaged over 40 microphones, e.g.

$$\overline{u'}(x, \frac{\Delta y}{2}, t) = \frac{1}{40} \sum_{i=1}^{40} u'(x, \frac{\Delta y}{2}, z_i, t), \quad (25)$$

with $(x, \frac{\Delta y}{2}, z_i)$ the position of the i -th microphone within an array. Time is made dimensionless by h'/c , with c the speed of sound and h' the dimensional duct height. The array-averaging is carried out in order to obtain the plane-wave components of the acoustic field (see^{9,11} for details).

The perturbations (on the mean flow variables) can be written in terms of left-travelling and right-travelling components. For the array-averaged pressure perturbation:

$$\overline{p'} = p^+ + p^-, \quad (26)$$

and for the array-averaged velocity perturbation:

$$\overline{u'} = (p^+ - p^-)/\rho_0 c_0, \quad (27)$$

where the mean density ρ_0 and the speed of sound c_0 are non-dimensional and equal to unity. With the help of equations (26) and (27) the reflection and transmission coefficients of the waves can be evaluated. For the linear problem considered we can write the reflection coefficient R , of the plane waves in region 2 as:

Higher-Order Discontinuous Galerkin Method for Aeroacoustic Wave Propagation on Distorted Grids

$$R = \frac{\overline{p_2'} - \rho_0 c_0 \overline{u_2'}}{\overline{p_2'} + \rho_0 c_0 \overline{u_2'}}, \quad (28)$$

where array-averaged pressure and velocity perturbations are $\overline{p_2'} = \overline{p'}(x = 0.5, y = \frac{\Delta y}{2}, t)$ and $\overline{u_2'} = \overline{u'}(x = 0.5, y = \frac{\Delta y}{2}, t)$, respectively, at the array in region 2 in which $z \in [1, 2]$. The transmission coefficient T , of the plane waves in region 1 can be expressed as:

$$T = \frac{\overline{p_1'} - \rho_0 c_0 \overline{u_1'}}{\overline{p_2'} + \rho_0 c_0 \overline{u_2'}}, \quad (29)$$

where array-averaged pressure and velocity perturbations are $\overline{p_1'} = \overline{p'}(x = 0.5, y = \frac{\Delta y}{2}, t)$ and $\overline{u_1'} = \overline{u'}(x = 0.5, y = \frac{\Delta y}{2}, t)$, respectively, at the array in region 2 in which $z \in [0, 1]$.

Reflection and transmission coefficients R and T are shown in figure (10) showing the ratios of the amplitudes of the reflected and transmitted plane waves that are plotted versus ω/ω_c for the present slit width of $s/(h/2) = 0.125$. Below the cut-off frequency $\omega_c = \left(\frac{2\pi c}{h}\right) = \pi$ we find an excellent agreement between numerical and analytical results. Please note that because we consider plane waves, below the cut-off frequency we have $R^2 + T^2 = 1$, from energy conservation. Above the cut-off frequency this relationship does not hold because energy is transferred to a higher non-planar mode.

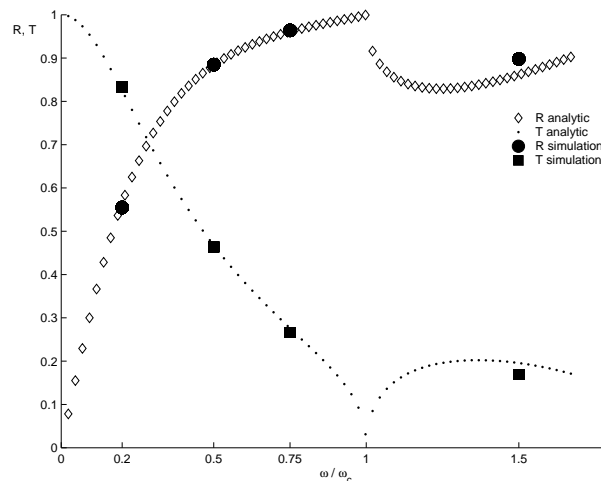


Figure 10. The ratios of the amplitudes of the reflected and transmitted plane waves versus ω/ω_c . (R : Ratio of the amplitudes of the reflected wave and the incoming wave in region 2. T : Ratio of the amplitudes of the transmitted wave in region 1 and the incoming wave in region 2). The analytic data is due to Kooijman^{19,20}.

In the left hand side of figure (11) contour plots are shown for the pressure perturbation in the plane $y = \Delta y/2$ for $t = 0.5$ to 7.5 excluding zero-level while in the right hand side the pressure perturbation including zero-level are plotted, all for $\omega = \frac{3}{4}\omega_c$, below the *cut-off* frequency. This data is for the mesh with $120 \times 1 \times 80$ elements in x -, y - and z -directions, respectively.

This data gives a clean overview of the diffraction of acoustic waves in the duct with the slitted flat plate without mean flow. The sine wave moves in from the left boundary and reflects from the plane of symmetry $x = L = 3$, with a reflected wave in region 2 and a wave moving into region 1. The reflected wave appears as a more or less planar wave, while the diffracted wave is much more two-dimensional.

The present method produces weak artificial waves of small amplitude. In the contour plots presented on the left-hand side of figure (11), they are not evident because in the contour levels we did not include the zero-level of the perturbation pressure and the amplitude of these waves is below the first positive and the first negative contour level. The right-hand side of figure (11) presents the contour plots including the zero-level. It shows that, originating from the slope-discontinuity at the front of the incoming wave, waves propagating at a higher speed than c_0 lead the acoustic wave and diffract at the slit in the plate.

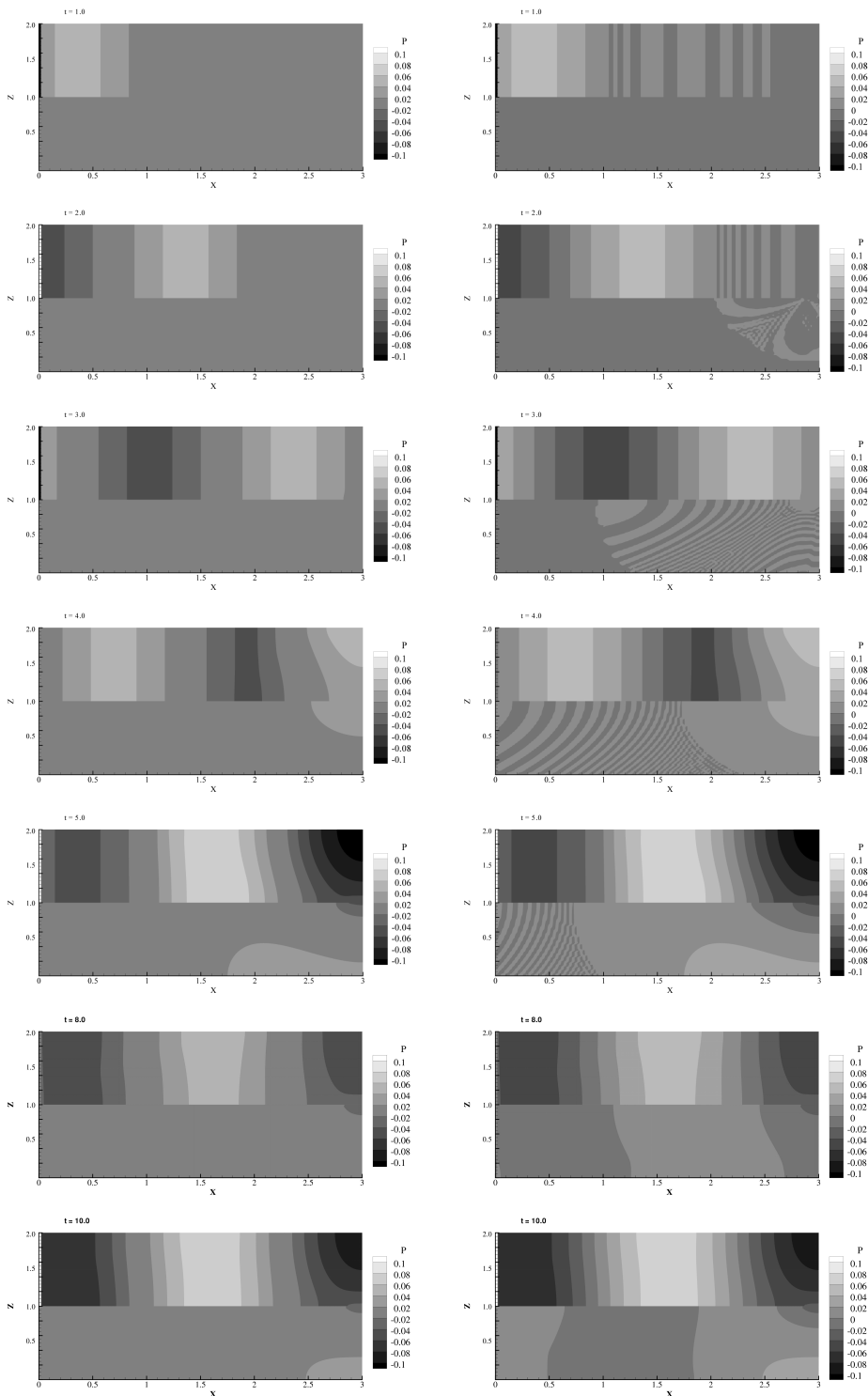


Figure 11. Contour plots for the pressure perturbation in the plane $y = \Delta y/2$ for $t = 1.0$ to 7.0 excluding zero-level (left) and including zero-level (right). ($\omega = \frac{3}{4}\omega_c$). $\Delta x = \Delta y = \Delta z = 0.025$, $\Delta t = 1.0 \cdot 10^{-3}$.

In the contour plots for $t = 8.0$ and $t = 10.0$ both on the left and right-hand side of figure (11) the effect of slope-discontinuity disappears since the artificial waves left the domain which are the only disturbance in the

Higher-Order Discontinuous Galerkin Method for Aeroacoustic Wave Propagation on Distorted Grids

flow field.

5.0 Concluding Remarks

The effect of grid distortion is investigated by considering two types of distorted grids: skewed and randomly distorted grids. For the skewed mesh the L_2 -norm of the error in the solution increases with increasing distortion α . The order of magnitude of the effect of grid distortion, for small grid distortions, is of the same order of magnitude as the difference between solutions for different mesh sizes. For the case of a randomly-distorted mesh the effect of the distortion on the difference between the solution with and the solution without distortion is relatively large. This is attributed to the fact that in the present implementation the mapping of the elements from physical to computational space is assumed to be linear, which contributes a second order term to the truncation error of the method. For the generic acoustic liner problem the results show that originating from the slope-discontinuity at the front of the incoming wave, waves propagating at a higher speed than c_0 lead the acoustic wave and diffract at the slit in the plate.

References

- [1] C. Johnson, J. Pitkärata, An analysis of the discontinuous galerkin method for a scalar hyperbolic equation, *Math. Comput.* 176 (1986) 1-26.
- [2] B. Cockburn, S. Hou, C.W. Shu, TVB Runge-Kutta local projection discontinuous galerkin finite element method for conservation laws II: general framework, *Math. Comput.* 186 (1989) 411-435.
- [3] H.L. Atkins, Continued development of the discontinuous galerkin method for computational aeroacoustic applications, AIAA paper 97-1581 (1997).
- [4] F.Q. Hu, M.Y. Hussaini and P. Rasetarinera, An Analysis of the Discontinuous Galerkin Method for Wave Propagation Problems, *Journal of Computational Physics*, Vol. 151, pp. 921-946, 1999.
- [5] C.P.A. Blom, R. Hagmeijer, A. Biesheuvel and H.W.M. Hoeijmakers, Three-dimensional Quadrature-free Discontinuous Galerkin Method for Computational Aeroacoustics, AIAA-Paper 2001-2198, 7th AIAA/CEAS Aeroacoustics Conference, Maastricht, May 2001.
- [6] C.P.A. Blom, R. Hagmeijer, E. Védy, Development of discontinuous galerkin method for the linearized euler equations, RTA/AVT Symposium on Development in Computational Aero- and Hydro-Acoustics, Manchester, UK (2001).
- [7] H. Özdemir, R. Hagmeijer and H. W. M. Hoeijmakers, Development of Higher-Order Discontinuous Galerkin Method on Hexahedral Elements, *Euromech Colloquium 449: Computational Aeroacoustics*, Chamonix, France, December 2003.
- [8] H. Özdemir, C.P.A. Blom, R. Hagmeijer and H. W. M. Hoeijmakers, Development of Higher-Order Discontinuous Galerkin Method on Hexahedral Elements, 10th AIAA/CEAS Aeroacoustics Conference, Manchester, UK, May 2004.
- [9] H. Özdemir, G. Kooijman, R. Hagmeijer, A. Hirschberg, H.W.M. Hoeijmakers, Validation of Higher-Order Discontinuous Galerkin Method for the Linearized Euler Equations, AIAA 2005-2821, 11th AIAA/CEAS Aeroacoustics Conference (26th AIAA Aeroacoustics Conference), Monterey, CA, USA, 2005.
- [10] H. Özdemir, R. Hagmeijer, H.W.M. Hoeijmakers, *Verification of Higher-Order Discontinuous Galerkin Method on Hexahedral Elements*, *Comptes Rendus Mecanique*, Vol. 333, pp. 719-725, 2005.
- [11] H. Özdemir, High-Order Discontinuous Galerkin Method on Hexahedral Elements for Aeroacoustics, PhD thesis, Department of Mechanical Engineering, Engineering Fluid Dynamics, University of Twente, 2006.

**Higher-Order Discontinuous Galerkin Method for
Aeroacoustic Wave Propagation on Distorted Grids**

- [12] F. Q. Hu and H. L. Atkins, Eigensolution analysis of discontinuous galerkin method with non-uniform grids, part I: one space dimension, *J. Comput. Phys.* 182 (2002) 516-545.
- [13] R. Hagmeijer, C.P.A. Blom and H.W.M. Hoeijmakers, Wave-Speed Analysis of Discontinuous Galerkin Finite Element Method for Aeroacoustics, *ECCOMAS Computational Fluid Dynamics Conference*, 2001.
- [14] A. Jameson, W. Schmidt, E. Turkel, Numerical solution of the Euler equations by finite volume methods using runge-kutta time-stepping schemes, *AIAA paper 1981-1259* (1981).
- [15] P. Lesaint, P.A. Raviart, On a finite element method for solving the neutron transport equation, *Mathematical Aspects of Finite Elements in Partial Differential Equations*, Academic Press 1974.
- [16] T. Peterson, A note on the convergence of the discontinuous galerkin method for a scalar hyperbolic equation, *SIAM J. Numer. Anal.* 28 (1991) 133-140.
- [17] G.R. Richter, An optimal-order error estimate for the discontinuous galerkin method, *Math. Comput.* 50 (1988) 75-88.
- [18] A.D. Pierce, *Acoustics. An Introduction to Its Physical Principles and Applications*, the Acoustical Society of America, New York, 1994.
- [19] G. Kooijman, Y. Aurégan and A. Hirschberg, Orifice Impedance under Grazing Flow: Modal Expansion Approach, *AIAA 2005-2857*, 11th AIAA/CEAS Aeroacoustics Conference (26th AIAA Aeroacoustics Conference), Monterey, CA, USA, 2005.
- [20] G. Kooijman, *Acoustical Response of Shear Layers*, PhD thesis, Technical University of Eindhoven, 2007.

Higher-Order Discontinuous Galerkin Method for Aeroacoustic Wave Propagation on Distorted Grids

Paper No. 40

Discussers' Name: Ch. Hirsch

Question:

- 1) On the distorted grids, have you verified the order of discretisation, when you refine the grid? It should remain the same as on the undistorted grid, although at a higher level of error.
- 2) What is the accuracy difference between the Lax-Friedrichs Riemann solver and other options, say a Roe solver?

Authors' Reply:

1) On the undistorted grid as well as on the skewed grid we have verified the order of the accuracy of the discretisation. Since we restrict the elements to be parallelepiped the transformation from physical to computational domain is linear. In case using non-parallelepiped elements, i.e. distorted grid, the linear transformation does not hold anymore and the truncation error becomes dominant.

2) For the solution of the Riemann problem the Lax-Friedrich flux formula and an exact characteristics splitting (the exact Roe solver) are both analytically analysed. Although in the literature it is shown that in case of exact characteristics splitting the superior node becomes non-existent, using Roe solver led to stability problems and we chose to use Lax-Friedrich flux formula with the quadrature-free implementation.

When the flow field can not be approximated with piecewise-constant assumption it is of course natural to use the quadrature formula in order to keep the order of the accuracy of the method in desired levels.